batteries

MDPI

Article

Multi-Objective Sizing Method for PV-BESS Integration with EV Charging Stations and Analysis Across Different Parking Scenarios

Francesco Maria Tiburtini [1], Francesco Lo Franco [2] and Mattia Ricco [1,*]

[1] Department of Electrical, Electronic, and Information Engineering "Guglielmo Marconi" (DEI), University of Bologna, 40136 Bologna, Italy; francesco.tiburtini2@unibo.it
[2] Syniergy S.r.l., 40128 Bologna, Italy; f.lofranco@syniergy.it
* Correspondence: mattia.ricco@unibo.it

Abstract

The growing adoption of electric vehicles (EVs) is driving the expansion of charging networks. Local photovoltaic (PV) systems combined with battery energy storage systems (BESS) have emerged as promising solutions to mitigate the impact of charging demand on the grid and reduce the environmental impact of EV charging. In this context, proper sizing of PV-BESS systems is crucial to maximize their integration with charging hubs (CHs) and ensure optimal performance. This paper proposes a multi-objective sizing method to optimize the energy and economic performance of PV-BESS systems in EV charging hubs. Sizing optimization is performed using a Non-Dominated Sorting Genetic Algorithm-II. The method is applied to four CH scenarios characterized by variations in energy demand, user behavior, and location. Results indicate that while optimal PV size remains relatively consistent across scenarios, the ideal BESS configuration varies with each scenario's characteristics. Optimized PV-BESS integration significantly improves energy performance, increasing system self-sufficiency by up to +72%. From an economic point of view, results show that in some cases, smaller BESS capacities are more advantageous due to lower capital costs, while in others, larger BESS sizes reduce overall costs by up to −50%, significantly cutting utility expenses despite higher initial investment.

Keywords: photovoltaic systems; battery energy storage systems; electric vehicles; charging stations; sizing optimization; multi-objective optimization

Academic Editors: Zhi Cao, Chris Mi and Naser Vosoughi Kurdkandi

Received: 20 October 2025
Revised: 5 November 2025
Accepted: 7 November 2025
Published: 17 November 2025

Citation: Tiburtini, F.M.; Lo Franco, F.; Ricco, M. Multi-Objective Sizing Method for PV-BESS Integration with EV Charging Stations and Analysis Across Different Parking Scenarios. *Batteries* **2025**, *11*, 422. https://doi.org/10.3390/batteries11110422

1. Introduction

The number of electric vehicles (EVs) is expected to grow significantly in the coming years as the transition to cleaner and more sustainable transportation accelerates. In Europe, according to [1], the share of electric vehicles is expected to rise to up to 38% by 2035. While EV represent a concrete solution for reducing pollutants and greenhouse gas emissions, this growth in EV share will lead to an increase in the number of charging hubs (CHs) needed to support EV load demand. However, the energy provided by the grid for EV charging is predominantly generated from fossil fuels rather than renewable sources [2]. The reliance on fossil-fuel-based grid power for charging undermines the potential of EVs to completely eliminate carbon emissions. Moreover, as reported in [3], the increasing number of charging stations may lead to higher peak demand in the coming years, potentially causing line and transformer overloads and stability problems within the distribution grid.

To mitigate these issues, the integration of local photovoltaic (PV) systems has proven to be a promising option, although it also presents certain challenges. Due to the inherent

intermittency of PV production, there may be a mismatch between energy generation and EV charging demands. This mismatch between production and load forces reliance on the grid to meet the load. For this reason, the integration of a battery energy storage system (BESS) with PV system can help reduce grid dependency by serving as an energy buffer, storing excess energy generated during the day and releasing it when the load exceeds generation, thereby reducing the environmental impact of EV charging and relieving stress on the distribution grid [3]. Moreover, the growing demand for clean transportation further emphasizes the need for sustainable energy solutions, especially when considering that some European countries are already moving towards mandatory installation of photovoltaic panels even for small-/medium-sized car parks [4]. For these reasons, it is essential to optimize the energy performance of the CHs, by minimizing the reliance on grid energy [5]. Moreover, ensuring the economic viability of the PV-BESS system is crucial for adoption by CHs stakeholders, making it important to consider both energy performance and financial feasibility. In this context, proper sizing of the PV-BESS system is crucial. It ensures optimal utilization of the PV-generated energy while minimizing operational costs. In fact, oversizing the system can lead to increased capital expenditures and reduced profitability, whereas undersizing risks system inefficiencies and potential failure [6].

Several studies have explored the optimal sizing of PV–BESS systems integrated with EV charging hubs. The optimal system size is determined by considering one or more objective functions. Among these, many works have employed cost-based indicators such as the Levelized Cost of Energy (LCOE) to evaluate system performance, representing the average cost of the energy supplied to EVs. For instance, Khawaja et al. [6] proposed an optimal cost-based model for grid-connected PV–BESS sizing, while Dai et al. [7] applied a particle swarm optimization approach to minimize LCOE. Other studies assessed economic performance through the annualized system cost: Liu et al. [8] analyzed PV–BESS integration in fast charging stations, including battery degradation, and Zhou et al. [9] proposed an optimization framework for smart households under different price mechanisms. Finally, Yan et al. [10] and Nafeh et al. [11] minimized the total system cost, which accounts for both investment and operating expenses over the system lifetime. On the other hand, energy performance has not been sufficiently explored. In fact, only a small number of studies have addressed this, but they do not take into account the specific load caused by EV charging. In ref. [12], an energy-based optimization approach to size integrated PV-BESS systems for residential and commercial settings is proposed. The target is to properly size the system to minimize buying and selling energy from/to the grid. The proposed methodology evaluates various PV and BESS configurations based on real annual load data, optimizing the amount of energy stored into the battery to reduce energy exchanged with the grid. The results demonstrate that PV-BESS systems can significantly reduce gross energy consumption, achieving reductions of approximately 80% for residential users and 40% for commercial users. However, this approach focuses only on energy optimization, without considering the system's economic performance. To achieve this, in ref. [13] the authors developed a sizing tool for hybrid PV-BESS systems aimed at optimizing both the energy and economic performance by minimizing both the degree of energy exchange with the grid and the cost of the investment. The study focuses on a building scenario and employs a particle swarm optimization algorithm to reduce computational time while providing efficient solutions. However, this study, like the previous one, does not specifically account for the load associated with electric vehicle charging, which is more variable and fluctuating than traditional building loads. In conclusion, none of the studies reviewed above has addressed the optimal sizing of PV-BESS systems integrated with EV charging hubs to optimize both energy and economic performance.

In addition, studies in the literature addressing the sizing of PV-BESS systems for EV charging hubs often fail to consider the specific characteristics of the CH location. Instead, most of these studies model the load of charging hubs as generic, without accounting for location specific factors that influence energy demand. For instance, Liu et al. [8] and Yan et al. [10] optimized photovoltaic and battery capacities for fast charging stations using predefined or stochastic EV arrival patterns, without distinguishing between different hub typologies. Similarly, Nafeh et al. [11] and Fang et al. [14] proposed techno-economic optimization models for PV–BESS systems, yet based their analysis on synthetic or generalized EV demand profiles instead of measured data representative of specific locations. This simplification ignores important factors, such as vehicle type, arrival time, charging power, and duration, which significantly impact energy demand [15]. To overcome this limitation, sizing of PV-BESS systems for CH integration must consider the unique load characteristics determined by the station's location. In this sense, in ref. [16], the authors proposed a multi-objective optimization approach aimed at reducing both the system cost and the pollutant emissions for the optimal sizing of PV-BESS system in a ultra-fast charging station of EVs, designed to serve EVs during medium- or long-distance travels, typically installed along motorways. The authors in ref. [17] focused on the optimal sizing of a PV-BESS system and its power management to minimize the overall energy cost. The effectiveness of the proposed model was demonstrated by considering as the load a charging hub with three EV chargers located at an office building. However, these studies consider only a single location, without comparing multiple scenarios that would allow an analysis of how the specific charging hub scenario impacts the optimal PV-BESS sizing. This gap highlights the need for a comparative approach to evaluate the influence of varying locations and operational conditions on optimal system configurations.

In the context of PV-BESS optimal sizing, accurately assessing the system's economic performance requires a precise calculation of the battery's lifetime, based on its characteristics and operation, as BESS related costs represent a significant portion of the system's total cost. However, many studies often overlook this or use simplified models. For instance, Leone et al. [16], Dai et al. [7], Islam et al. [18], and Alshammari et al. [19] assumed fixed battery lifetimes of 20, 10, 4, and 25 years, respectively, irrespective of the actual operating conditions. While this approach simplifies the analysis, it is sub-optimal because it does not take into account the actual effects of operating conditions. The latter have a significant impact on the actual life of a battery and therefore on its economics and replacement schedule. By using a fixed lifetime assumption, the analysis may overestimate or underestimate the economic performance of the system, leading to inaccurate conclusions and potentially suboptimal system designs. In the literature, battery lifetime estimation models were proposed. In [6], battery degradation is modeled using a simple annual percentage factor, applied uniformly to calculate the available capacity over time. However, this approach does not account for key operational variables such as charge/discharge cycles, depth of discharge, thereby limiting its accuracy. In ref. [20], the battery lifetime is estimated using a simplified approach that calculates the number of cycles based on cumulative SOC variations and a fixed depth of discharge of 80%. The battery is considered exhausted once the number of cycles reaches 3000, while this method is computationally efficient, it lacks accuracy as it does not account for variations in depth of discharge across different cycles, which have a varying impact on the overall battery lifetime. The model calculates cyclical degradation, but in addition to usage cycles, battery degradation is also influenced by periods of inactivity during which the battery is not in use. This type of degradation is known as calendar aging, and it is influenced by factors such as temperature, downtime duration, and state of charge during downtimes, further impacting the overall battery life. In this sense, the authors in ref. [17], in addition to cyclic degradation, propose a model

where calendar degradation is treated as a fixed parameter, set at 2% per year, while this approach simplifies the analysis, it overlooks the potential fluctuations in calendar degradation that may arise from operational factors, thus failing to capture its variability over time. In conclusion, generally, BESS lifetime loss is ignored or simplified in several studies concerning the sizing of PV-BESS systems integrated with EV charging hubs. However, since the BESS replacement cost represents a significant expense over the system's lifetime, it is necessary to establish a precise BESS model that takes into account this loss.

To the best of the author's knowledge, none of the reviewed papers addresses the multi-objective sizing optimization of PV-BESS systems combined with EV charging hubs, considering both energy and economic performance. Furthermore, the papers analyzed in this context consider either a generic CH load or a single CH site load, but do not consider multiple CH sites simultaneously. Finally, the literature review revealed that papers often fail to accurately estimate the lifetime of BESS, taking into account its characteristics and operation. To address these current limitations regarding the sizing optimization of PV-BESS systems integrated with EV charging hubs aiming to maximize both energy and economic performance, this paper proposes a framework to maximize, on one side, the energy independence of the CH from the grid, and on the other side, to maximize the economic profitability for the CH's stakeholders by minimizing the cost of the energy supplied to EVs. Furthermore, various charging locations are evaluated to explore a wider range of scenarios in various real-world contexts enabling an assessment of the impact on system sizing and performance across different scenarios. The EV power demand is calculated using a probabilistic approach based on real-world data on vehicle arrival and departure times from four different car parks, specifically, a paid public car park, a workplace car park, a municipal car park, and a mall car park. Finally, to improve the accuracy of BESS lifespan estimation compared to previous studies, a BESS degradation model is proposed that estimates battery life by considering both cyclic and calendar degradation based on real operating conditions. Photovoltaic power production data were sourced from the Photovoltaic Geographical Information System (PVGIS) to obtain realistic solar generation with a time resolution of 15 min. To simulate the power exchange between the system components, a battery power flows model has been developed. This model aims for evaluating the performance of the PV-BESS system, as it enables the calculation of energy flows and SOC variations. Finally, the resulting multi-objective optimization problem is solved using a metaheuristic approach. To identify the most suitable method for this class of problems, three state-of-the-art multi-objective algorithms are compared: Non-dominated Sorting Genetic Algorithm II (NSGA-II), Multi-Objective Evolutionary Algorithm based on Decomposition (MOEA/D), and Multi-Objective Particle Swarm Optimization (MOPSO). A comprehensive statistical analysis demonstrates that NSGA-II achieves superior stability and computational efficiency while maintaining equivalent Pareto front quality to competing approaches, making it the reference algorithm for system sizing across all scenarios.

The rest of the paper is organized as follows. Section 2 presents the data used for the simulation, the battery power flows model, and the degradation model. In Section 3 the objective functions are presented and the multi-objective problem is defined. Energy and economic results are presented and described in Section 4. Finally, Section 5 presents the conclusions.

2. System Modeling

In this section, the system under study is introduced, providing a full overview of the key components involved. Figure 1 shows the system under analysis that comprises a photovoltaic plant, generating the PV power P_{PV}, a charging hub with multiple EV

charging points, consuming the load power P_{EV}, and a battery storage system, which can provide the power P_B as a buffer between generation and load. The system elements are connected and exchange power with the external grid, designated as P_G. The following balance equation holds:

$$P_{PV} - P_{EV} + P_B = P_G \quad (1)$$

where P_B is defined as negative during charging and positive during discharging of the BESS. P_G is assumed negative when the power is injected to the grid and positive when consumed.

The objective of this section is to present a method for modeling each element of the system in terms of power flows. In order to accurately assess the variability of the photovoltaic source, it is essential to consider both seasonal and daily fluctuations. Consequently, a minimum time horizon of one year is required for analysis. To also take into account the intermittency of both load and production, a 15-min resolution is adopted. In the following, Section 2.1 models and calculates the PV production, Section 2.2 focuses on the EV load, and Section 2.3 addresses the BESS operation with 15-min resolution for a one-year time range. In addition to analyzing power flows, it is essential to examine the price values of the energy exchanged with the external grid in order to conduct a comprehensive economic assessment. Finally, to obtain meaningful economic results from the optimization algorithm, the energy price profiles and consequently the grid energy cost model are developed in Section 2.4.

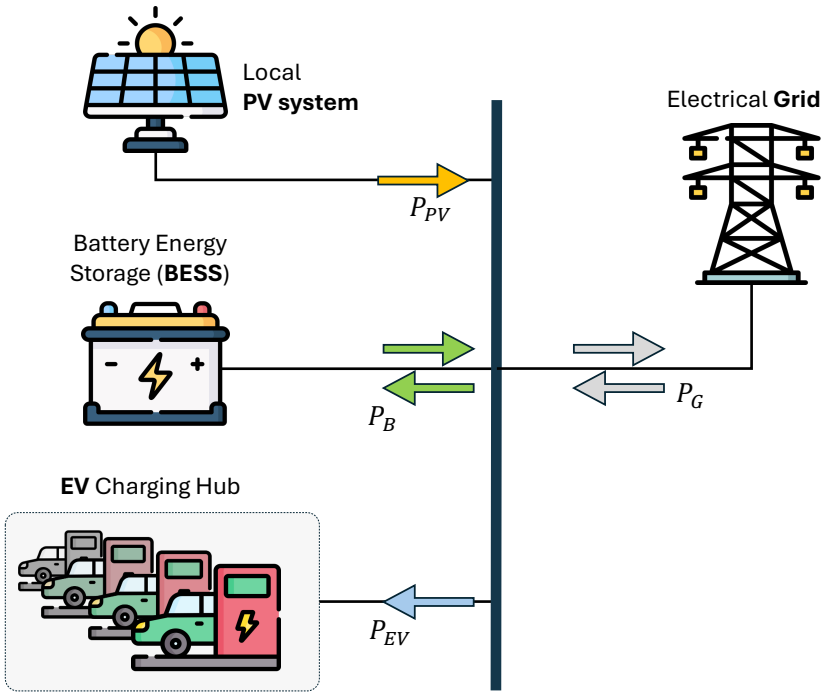

Figure 1. Reference scenario and nomenclature of the power flow for each element.

2.1. PV Power Profile Modeling

The PV power profile $P_{PV}(t)$, can be calculated using the following equation:

$$P_{PV}(t) = S_{PV}\bar{P}_{PV}(t) \quad (2)$$

where S_{PV} represents the peak power of the system, which is equivalent to the PV size in kWp. The variable $\bar{P}_{PV}(t)$ is the normalized power profile, expressed as a function of its peak power (kW/kWp). In other words, $\bar{P}_{PV}(t)$ denotes the power profile of a 1 kWp PV

system. By employing Equation (2), it is possible to assess the power profile of PV plants with different sizes by varying S_{PV}, but nevertheless keeping $\bar{P}_{PV}(t)$ unchanged.

The normalized power profile can be calculated from environmental data, such as irradiance and temperature. One of the most commonly used models for calculating photovoltaic output is expressed in Equation (3) [21]:

$$\bar{P}_{PV}(t) = \frac{G(t)}{G_{STC}}[1 + \gamma(T_{cell}(t) - T_{STC})]\eta_{loss} \quad (3)$$

where $G(t)$ is the global irradiance profile (W/m^2) on the PV-array plane (inclined plane), T_{cell} is the operating temperature of the PV cell (°C), G_{STC} and T_{STC} are the irradiance and cell temperature under standard test condition, respectively, 1000 W/m^2 and 25 °C. The temperature coefficient γ represents how much the nominal power varies with respect to cell temperature, and is usually between $-0.3\%/°C$ and $-0.5\%/°C$ for many silicon photovoltaic modules. Furthermore, the η_{loss}-coefficient take into account the conversion losses from the DC to AC side of the system.

The cell temperature is related to the ambient temperature (T_{amb}) and can be estimated using the following formula:

$$T_{cell}(t) = T_{amb}(t) + \frac{G(t)}{G_{NOCT}}(T_{NOCT} - 20\,°C) \quad (4)$$

where T_{NOCT} is the Nominal Operating Cell Temperature (NOCT), which is a standard measure describing the cell temperature under irradiance of G_{NOCT} = 800 W/m^2 and ambient temperature of 20 °C. The values of both γ and T_{NOCT} can be readily derived from the module data sheet. It is worth noting that non-optimal operating conditions, such as module mismatch, partial shading, or hotspot effects, were not explicitly modeled in this work. Their influence could be represented by introducing a correction factor into Equation (3), modifying the overall PV efficiency to account for additional losses.

In order to conduct a one-year analysis with a sufficient level of resolution, data from the Photovoltaic Geographical Information System [22] are retrieved. PVGIS is a free and open-access tool that allows the assessment of photovoltaic output based on historical meteorological data. All PVGIS tools can be accessed via web APIs, and the information required for Equation (3) model can be retrieved by setting the PV system parameters, such as the location of the plant, the tilt angle of the PV arrays, the PV system losses, and so forth. Table 1 shows the setting of the main parameters used to calculate the normalized PV profile. The T_{NOCT} and γ parameters are retrieved from ref. [23], whereas the system losses are set in accordance with ref. [24].

Table 1. Setting of the PV model parameters.

Parameter	Value
Location	Bologna, Italy
Tilt angle	30°
Azimuthal orientation	South
Weather database	PVGIS-SARAH2
PV-cell technology	Crystalline Silicon
NOCT temperature (T_{NOCT})	45 °C
Temperature coeff. (γ)	$-0.45\%/°C$
Percentage system losses	14%

Finally, Figure 2 illustrates one year of the $\bar{P}_{PV}$ profile with 15-min resolution, taking into account the weather historical data from 2023 and the settings outlined in Table 1.

The figure demonstrates the incorporation of both seasonal and daily power variability in the proposed PV model.

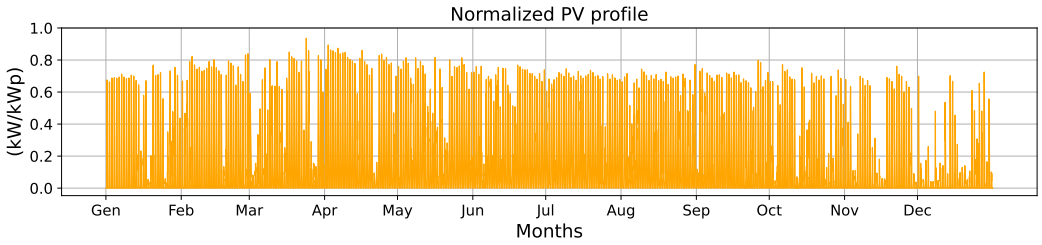

Figure 2. One-year $\bar{P}_{PV}$ power profile with 15-min resolution based on historical weather data from 2023.

2.2. EV Charging Demand Modeling

A reasonable prediction of the load profile is necessary to accurately address the sizing optimization problem. EV demand profile may depend on multiple factors such as the number of daily users and their behavior in terms of arrival, departure and parking time. The power rating of the charging infrastructure may affect the peak power and the charging session duration, as well as the characteristics of the EV models in terms of maximum charging rate. The objective of this Section is to calculate the power demand of a charging hub, designated as P_{EV}, over one-year period with a resolution of 15 min. For this purpose, the algorithm developed in ref. [15] is adapted and employed in this work. The algorithm uses a probabilistic approach to generate realistic load profiles by analyzing real-world data on vehicle arrival and departure times for various parking scenarios. These patterns are reconstructed based on probabilities to reflect typical user behavior. A similar approach is employed to estimate the initial SOC of EVs upon their arrival at the charging hub and their energy demand. Additionally, an EV battery charging behavioral model is also implemented in ref. [15] to account for the different charging characteristics of various EV models.

As reported in ref. [15], users' behavior can significantly change depending on the parking scenario. These differences in arrival and parking times are reflected in the charging hub's load profile. Starting from a data collection campaign carried out on several parking lots located in the urban area of Bologna, some of the most common urban scenarios are analyzed and described below:

- Paid public car park: in urban contexts, such as city center car parks, the distribution of arrival and departure times is more concentrated during daytime hours. Users may arrive at different times of the day, either for work activities or for leisure or shopping purposes. However, data indicate a slight increase in users' arrivals during the morning and evening peak hours. The average parking time is approximately 120 min.
- Working place car park: this scenario refers to typical parking lots in company or office areas, where usage follows a routine aligned with standard working hours. Consequently, arrival and departure time presents a well-defined pattern. Most arrivals are concentrated in the early morning hours, with the majority of departures in the late afternoon. The average parking time is about 6 h.
- Municipal car park: this scenario concerns a municipal public car park, with users arriving at different times of the day. It presents similar arrival and departure profiles to the previous city car park, with user numbers increasing during traffic peak hours. However, the data set presents a higher variance and longer parking times, with an average duration of 140 min.
- Mall car park: in this scenario, there is a high flow of users during the daytime, with a moderate increase in the evening hours. The average parking duration is shorter than in previous scenarios, around 60 min, as users tend to park for shopping or brief visits.

The input settings of the EV load demand model proposed in ref. [15] are as follows: the number of users per day (N_{EV}), i.e., the number of daily charging sessions; the car park scenario; and the maximum power rating available at the charging point (P_{CP}). It should be noted that the resulting CH load profile, given by the sum of each charging session power, can present significant changes as the input settings change. For each scenario, a trade-off value of P_{CP} is determined to ensure users have an adequate SOC at departure, while preventing oversizing of the charging infrastructure's power capacity. This value is evidently higher for scenarios with a lower average parking time. The characteristics of the charging point infrastructure are then set according to reference [15] and reported in Table 2.

The algorithm permits the calculation of EVs' load profile on a daily basis; however, the analysis proposed in this paper is on an annual basis. Consequently, a typical week is reconstructed from the daily profiles, which are then repeated to generate the annual profile. In a typical week, the number of daily users entering the parking facilities is distributed according to weekdays and weekends. On weekends, entrance data shows an increase of 4% and 51% for the paid public car park and mall car park scenarios, respectively, while a decrease of 33% is found for the municipal car park. With regard to working place car park, it is assumed that the company is closed during the weekend, and therefore no charging is recorded.

The number of daily charging sessions is determined according to the size and traffic of the car park in terms of daily entrances. Three cases are considered in this work. In the small-size case, a car park with an average of 100 users/day is considered, while 200 users/day and 400 users/day are considered in the medium- and large-size cases. The number of EV users is obtained by considering an EV penetration share of 7%. This value corresponds to the projected share of EVs in Europe in 2025, as analyzed in ref. [1]. This results in $N_{EV} = 7$, 14 and 28 charging sessions per day on a weekly average for the small-, medium- and large-case, respectively. The weekly charging load profiles for the different parking scenarios and sizes are shown in Figure 3.

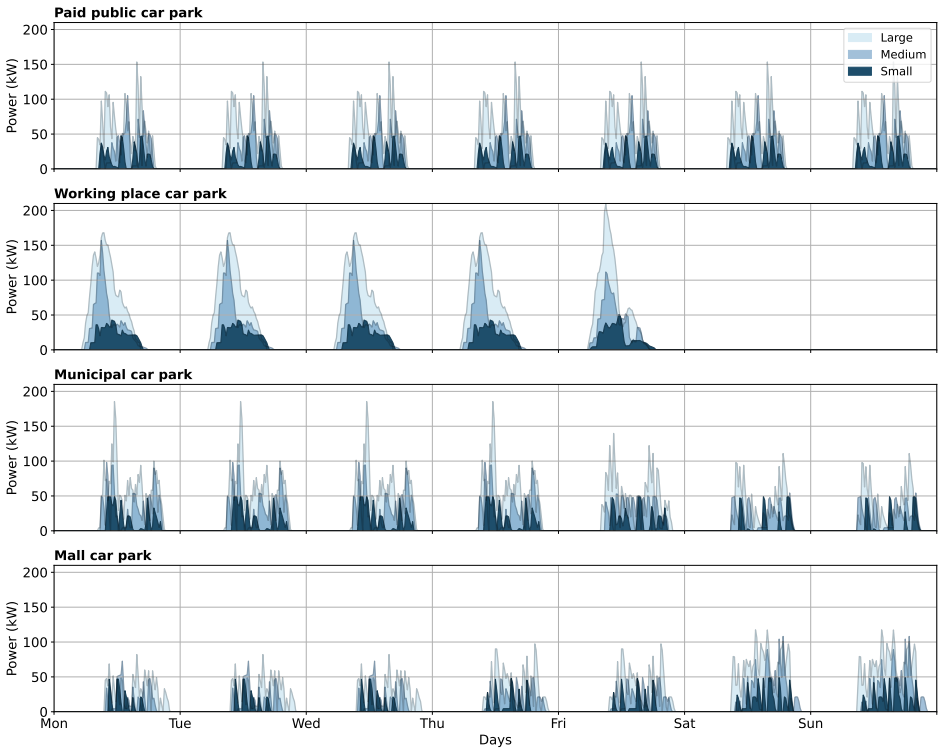

Figure 3. Weekly EV charging load profiles for different parking scenarios and lot sizes.

Table 2. Description of the reference CH scenario as a function of the car park scenario, the charging points power rating, the number of charging sessions per day, and average daily energy demand.

Car Park Scenario	Scenario	P_{CP} (kW)	N_{EV} (Daily)	Energy Demand (kWh/Day)
Paid public	small	22	7	197
	medium	22	14	393
	large	22	28	603
Working place	small	22	7	197
	medium	22	14	355
	large	22	28	661
Municipal	small	22	7	203
	medium	22	14	410
	large	22	28	602
Mall car park	small	50	7	182
	medium	50	14	417
	large	50	28	654

2.3. BESS Modeling

The BESS acts as a buffer between generation and load. When PV generation is higher than the load demand, the BESS can store excess power (charging phase); conversely, the BESS can provide energy to the load in the case of low PV power availability or higher demand (discharging phase). Considering Equation (5), the ideal BESS operation is achieved when there is no power sharing with the external grid, or, in other words, when:

$$P_B^*(t) = P_{EV}(t) - P_{PV}(t) \tag{5}$$

where P_{B}^* is the ideal battery power. However, in BESS modeling, it is essential to account for the constraints imposed by the maximum power rating of the storage system during both the charging and discharging phases, i.e., $-P_{\mathrm{B}}^{\max} \leq P_{\mathrm{B}} \leq P_{\mathrm{B}}^{\max}$. Furthermore, it is crucial to consider the limitations related to the maximum state of charge ($SOC_{\max}$) during charging and the minimum state of charge ($SOC_{\min}$) during discharging. Then Equation (5), which represents the ideal buffer operation, is modified as follows.

$$P_{\mathrm{B}} = \begin{cases} \min(P_{\mathrm{B}}^*, P_{\mathrm{B}}^{\max}) & \text{if } P_{\mathrm{B}}^* > 0 \text{ and } SOC > SOC_{\min} \\ \max(P_{\mathrm{B}}^*, -P_{\mathrm{B}}^{\max}) & \text{if } P_{\mathrm{B}}^* < 0 \text{ and } SOC < SOC_{\max} \\ 0 & \text{otherwise} \end{cases} \tag{6}$$

The maximum power rating is calculated as a function of the maximum charging rate (C_{R}) and the nominal capacity of BESS (S_{B} in kWh). C_{R} indicates the maximum charging and discharge rate (in h^{-1}) related to the nominal battery capacity. The maximum power of the system is obtained as follows: $P_{\mathrm{B}}^{\max} = C_{\mathrm{R}} S_{\mathrm{B}}$. The typical C_{R} for stationary storage applications ranges between 0.2C and 1C [25]. According to ref. [20], in this paper $C_{\mathrm{R}} = 0.5$ is assumed, which indicates that the battery can be fully charged or discharged in two hours. The usable capacity of the battery is typically limited by the manufacturer to prevent effects and damage due to overcharging and over-discharging events as described in ref. [26]. Equation (6) allows the SOC to remain within the permissible values, i.e., $SOC_{\min} = 5\%$ and $SOC_{\max} = 95\%$.

The SOC used in Equation (6) is obtained through time-step integration of the battery power, as shown in Equation (7):

$$SOC(t+1) = SOC(t) + \frac{P_B(t)\Delta t}{S_B} \tag{7}$$

where Δt is the simulation time step, set to 15 min in this study.

Finally, in order to integrate conversion losses into the BESS model, this work employs the approach proposed in ref. [27]. The losses associated with the round-trip efficiency of the battery are modeled as follows. Let P_B be the power measured at the DC terminals of the BESS, and η_B the battery efficiency during the charging or discharging phase, the power ideally measured inside the battery cell (P_B^{ins}) is given by the following equation.

$$\begin{cases} P_B^{ins} = \dfrac{1}{\eta_B} P_B & \text{if } P_B > 0 \text{ (discharging)} \\ P_B^{ins} = \eta_B P_B & \text{if } P_B < 0 \text{ (charging)} \end{cases} \tag{8}$$

Due to battery losses, the model expressed by Equation (8) results in a higher internal energy consumption during the discharge phase and a lower energy incoming during the charging phase compared to the energy measured at the battery terminals. In practice, this has an impact on the SOC trend, which demonstrates a reduction in growth during the charging phase and an increased rate of reduction during the discharging phase compared to the ideal case. In this paper, it is assumed that the battery efficiency is the same for both charging and discharging. The parameter η_B is derived from the battery's round-trip efficiency, designed as η_{B-RT}, which measures the energy losses occurring throughout a complete charge-discharge cycle. For a stationary battery system operating at 0.5 C, the round-trip efficiency is typically around 90% [27,28]. Since the round-trip efficiency reflects the performance over a complete charge-discharge cycle, it can be assumed to be the product of the individual efficiencies of the charge and discharge processes, then efficiency used in Equation (8) is obtained from $\eta_B = \sqrt{\eta_{B-RT}}$.

BESS Degradation Model

A precise calculation of the battery's lifetime, based on its characteristics and operation, allows a more accurate assessment of the system's economic performance. During its use, the battery is subject to a reduction in its usable capacity. In general, the BESS is considered to have reached the end of its useful life when its usable capacity is reduced by 20% of its nominal value [29]. The lifetime of a BESS (y_B) is highly dependent on battery usage and cell technology. In this study, a $LiFePO_4$ battery storage is considered as it is one of the most widely used technologies for stationary energy storage due to its excellent chemical and thermal stability and low cost [30].

For the same load demand and generation, the size of the BESS will have a significant impact on the battery's cycling and consequently its degradation rate. For example, a smaller capacity BESS is likely to experience more frequent cycling with higher depths of discharge compared to a larger capacity system. Therefore, a battery degradation model is proposed below to incorporate BESS lifetime considerations into the sizing optimization problem. The proposed degradation model is adapted from ref. [29] and consists of two components:

$$C_D = C_D^{cal} + C_D^{cyc} \tag{9}$$

where C_D is the total capacity degradation expressed as a percentage of the nominal capacity, C_D^{cal} is the calendar capacity degradation and C_D^{cyc} the cyclical capacity degradation.

The algorithm used to calculate the capacity degradation, and thus to estimate the BESS lifetime, is summarized in Figure 4.

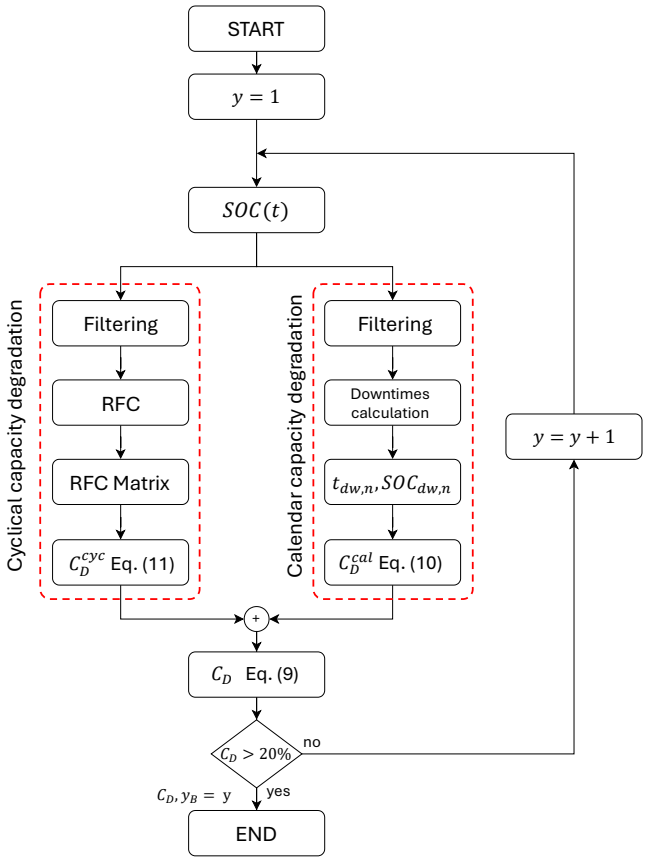

Figure 4. BESS degradation model flowchart.

Starting from the annual SOC profile obtained from the BESS model described in Section 2.3, the proposed algorithm calculates the parameters required to estimate the two degradation components. Using Equation (9), it evaluates the degradation accumulated during the y-th year. The iteration is repeated for subsequent years until the total degradation exceeds 20%. At this point, the algorithm stops and records both the level of degradation achieved and the time taken to reach it, which defines the operational lifetime of the system.

Figure 4 summarizes the 2 main branches of the degradation. The right branch shows the calculation of C_D^{cal}, which represents the loss of battery capacity that occurs during extended downtime. The downtime t_{dw} is defined as the time that the battery remains unused at a constant state of charge (SOC_{dw}). Calendar degradation increases with high temperatures, elevated SOC_{dw}, and extended t_{dw} durations [29]. To simplify the degradation model, a constant temperature of 25 °C is considered, as reported in ref. [29]. On the other hand, the dependence on SOC_{dw} and t_{dw} is derived via Equation (10).

$$C_D^{cal} = \sum_{n=1}^{N^{cal}} K_{cal} \cdot e^{0.0074 \cdot SOC_{dw,n}} \cdot \left(t_{dw,n} + t_{dw,n-1}^{eq}\right)^{0.8} \quad (10)$$

Equation (10) allows summing the n-th calendar degradation events that occur with different SOC_{dw} and t_{dw} (expressed in months). N^{cal} represents the total number of calendar degradation events, while $K_{cal} = 0.1723$ month^{-1} is a coefficient that depends on the operating temperature of the battery [31]. Since battery degradation is a non-linear process, simply adding up the capacity degradation of successive events leads to significant

discrepancies with respect to the actual degradation behavior of the battery. To overcome this limitation, this paper employs the superposition method, as proposed in ref. [32]. This method consists of considering the capacity degradation obtained in previous events (i.e., up to $n-1$) as an equivalent downtime. The equivalent downtime $t^{\mathrm{eq}}_{\mathrm{dw},n-1}$ is then added to the downtime of the n-th event in Equation (10).

The individual $SOC_{\mathrm{dw},n}$ and $t_{\mathrm{dw},n}$ values are obtained by processing the state of charge profile through two filtering steps. The first step employs a hysteresis filter that removes small variations in SOC values (less than 5%) by smoothing them to the previous value. The second step applies a binning process, discretizing the SOC values into predefined intervals, such as increments of 5%. The algorithm calculates each value of $t_{\mathrm{dw},n}$ and its relative $SOC_{\mathrm{dw},n}$, explicitly excluding instants when the SOC changes. Finally, the total $C^{\mathrm{cal}}_{\mathrm{D}}$ is obtained by Equation (10).

On the other hand, $C^{\mathrm{cyc}}_{\mathrm{D}}$ is directly related to the BESS cyclic operation, i.e., the charge and discharge phase that occurs during battery usage. A charge/discharge cycle is defined as a process in which the SOC starts from an initial value SOC_i, reaches a final value SOC_j, and returns to the same initial value SOC_i. Each cycle represents a degradation event $C^{\mathrm{cyc}}_{\mathrm{D},ij}$, whose intensity depends on the cycle depth of discharge $DOD_{ij} = |SOC_j - SOC_i|$, the average state of charge of the cycle SOC^{avr}_{ij}, and the temperature. According to ref. [32] the total cyclical capacity degradation is obtained by Equation (11):

$$C^{\mathrm{cyc}}_{\mathrm{D}} = \sum_{ij} K_{\mathrm{cyc}} \cdot e^{-0.019 \cdot SOC^{\mathrm{avr}}_{ij}} \cdot DOD^{0.716}_{ij} \cdot \left(nc_{ij} + nc^{eq}_{i-1,j-1}\right)^{0.5} \tag{11}$$

where K_{cyc} is a cyclic temperature coefficient and is equal to 0.021 considering an operating temperature of 25 °C [29]. For each pair SOC_i and SOC_j that characterizes the cycle, the total number of cycles, called nc_{ij}, is calculated. As for the calendar aging, the cyclical degradation accumulated from previous events (i.e., up to $i-1$, $j-1$) is considered by adding up an equivalent number of cycles $nc^{eq}_{i-1,j-1}$ to the current number of cycles in Equation (11).

The cyclic capacity degradation calculation is summarized in the left branch of the flowchart in Figure 4. The number of cycles nc_{ij} is obtained by the Rain-Flow Counting (RFC) method. The battery's SOC profile undergoes pre-processing before applying the RFC algorithm: an hysteresis filter removes small SOC fluctuations (<5%) to reduce noise; then a peak detector algorithm identifies maximum and minimum SOC values to mark transitions; finally, a binning process groups detected peaks into 5% SOC intervals for better cycle classification.

After this pre-processing step, the RFC method is employed. This method is generally used to calculate the number of cycles as reported in refs. [33–35]. The RFC algorithm processes four consecutive SOC points to detect cycles. If the two middle points fall between the first and last points, a valid cycle is identified. For a valid cycle, start and end SOC values, i.e., SOC_i and SOC_j, are recorded and the two middle points are removed from the SOC profile. If not valid, the next group is analyzed. The process continues until there are not enough points to form a loop.

All identified cycles are recorded in the RFC matrix, which is organized as follows: the rows identify the SOC levels at the start of the cycle (i.e., $SOC_i \in [5-95\%]$), while the columns identify the SOC levels at the end of the cycle (i.e., $SOC_j \in [5-95\%]$). Each cell of the RFC matrix indicates the number of cycles nc_{ij} between specific SOC start and end levels. Starting from the RFC matrix, it is possible to obtain the element of Equation (11) for each pair ij. Figure 5 provides an example of the RFC matrix, along with a graphical explanation of the method used to determine the parameters in Equation (11) for calculating cyclical capacity degradation.

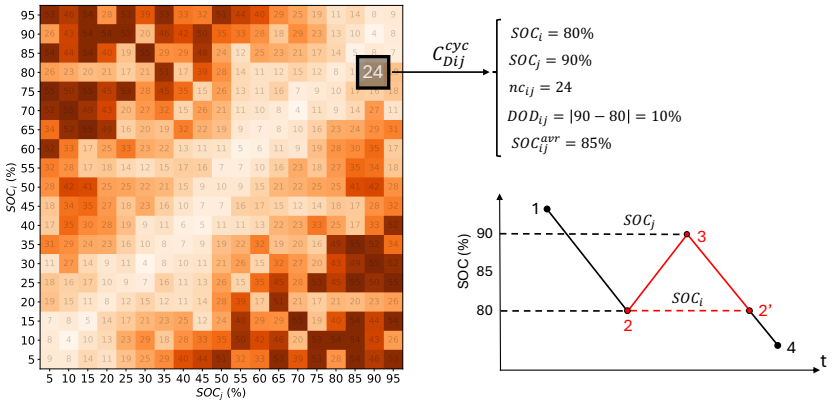

Figure 5. Example of RFC matrix and cycle parameter extraction. The color scale indicates the number of cycles ($n_{c_{ij}}$) in each matrix cell, while the red line represents an example of a charge–discharge trajectory.

It should be noted that only battery capacity degradation is considered in this study. Although the increase in internal resistance also contributes to battery aging by reducing the maximum deliverable power, previous works on $LiFePO_4$ cells have shown that when the capacity fade reaches 20% (end of life), the corresponding power fade remains below 5% [31]. Therefore, internal resistance growth was neglected to limit model complexity and computation time. However, this phenomenon can be modeled as a progressive decrease of $P_B^{\max}$, as formulated in ref. [31].

2.4. Grid Economic Exchange Modeling

In addition to the energy aspects discussed in the previous sections, this paper also addresses optimization from an economic perspective. Starting from the energy flows, it is therefore necessary to develop a model that takes into account the costs associated with the exchange of energy with the grid, including the costs of imported energy (purchased from the grid) and the revenue from injected energy (sold to the grid). Considering a one-year analysis, Equations (12) and (13) represent the calculation of the energy cost (C_G^+) and revenue (C_G^-), respectively:

$$C_G^+ = \int_{T=1\text{ year}} c_{\text{buy}}(t) \cdot P_G^+(t)\, dt \tag{12}$$

$$C_G^- = \int_{T=1\text{ year}} c_{\text{sell}}(t) \cdot P_G^-(t)\, dt \tag{13}$$

where c_{buy} and c_{sell} are the specific price of the imported and injected energy in EUR/kWh, while $P_G^+(t)$ and $P_G^-(t)$ are the profile of the grid imported and injected power, respectively.

The specific price c_{buy} is obtained from the data provided by the Italian Power Exchange—IPEX [36]. In this paper, we consider a purchase price based on the National Single Price (NSP) following Time-Of-Use (TOU) tariffs. The TOU tariffs typically have higher prices during peak hours, when demand is high and the grid is overloaded, and lower prices during off-peak hours, when demand decreases. In Italy, the energy market follows this structure by dividing the day into different price bands, such as "peak hours", "intermediate hours", and "off-peak hours". These bands correspond to specific time windows and days of the week. Additional costs, including network charges, taxes, and levies (e.g., value added tax, renewable, capacity, and environmental taxes), are included in c_{buy} according to refs. [37,38]. Fixed costs associated with contractual power were not included, as they are constant with respect to the optimization variables and thus do not affect the results.

On the other hand, the c_{sell} price depends on the adopted market mechanism. In Italy, it is generally managed by the national energy services operator, which applies either a fixed or a variable tariff depending on the market mechanism. The variable tariff is linked to the NSP for each geographical zone and follows TOU pricing. To ensure methodological generality and alignment with real market-based remuneration mechanisms, this study adopted a zonal NSP-based dynamic price.

In this paper, the annual variation of the price profiles is considered, with a 15-min resolution to match that adopted for the power profiles. Figure 6 shows the c_{buy} and c_{sell} price profiles for 2023. The annual view illustrates the monthly price variations, while a detailed weekly view highlights the daily fluctuations, showing that the purchase price follows the TOU tariff and the NSP varies on an hourly basis.

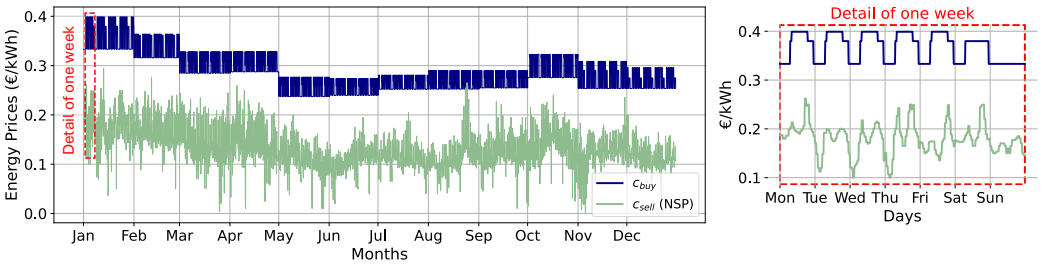

Figure 6. Annual and weekly energy price profiles.

3. PV-BESS Sizing Optimization Problem

Figure 7 shows an example of the power flow profiles of each element of the system over a one week period. A preliminary size setting of S_{PV}=100 kWp and S_{B} = 100 kWh is selected to support the EV charging load of the paid "public car park" (medium size) scenario.

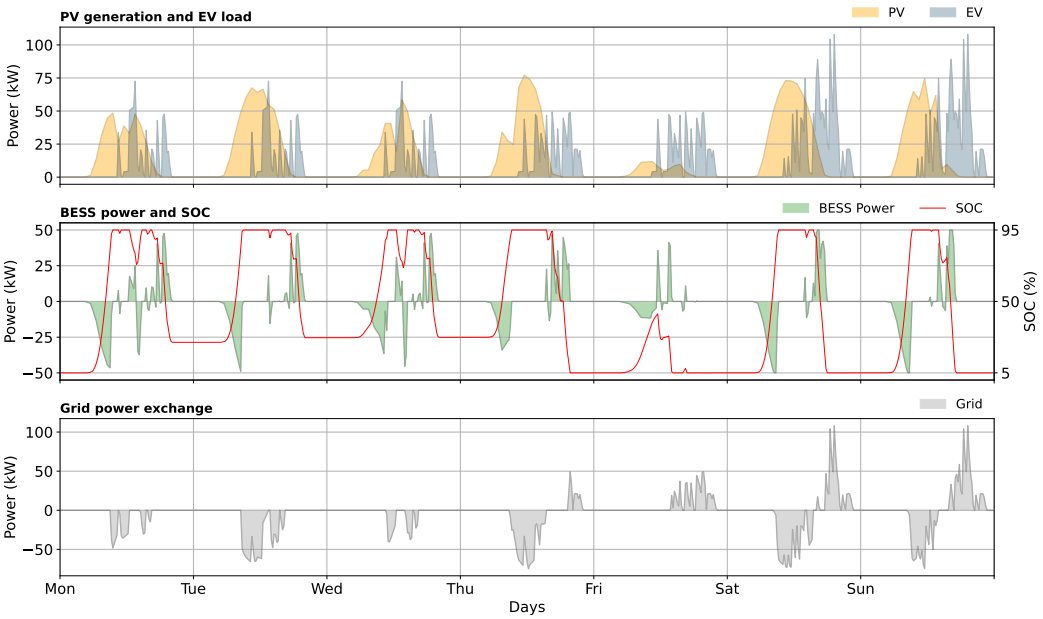

Figure 7. System power flow profiles: at the top is the PV power and the load. In the middle is the SOC and BESS power, and below is the power exchanged with the grid.

The top frame in Figure 7 shows the PV power profile in orange and the total EV load profile in blue. The output of the BESS model is shown in the middle frame: the green profile depicts the BESS power, while the red line shows the BESS SOC evolution. According to the BESS model of Equations (5) and (6), the BESS power is negative/positive during the charging/discharging phase and depends on the balance between generation

and load. The SOC profile shows that its cyclicity is highly dependent on the balance between P_{PV} and P_{EV}. Under conditions of abundant production or low demand, it can reach high values. Conversely, under conditions of low production, it can remain at low values for long periods. The parameters that affect BESS degradation, such as charge-discharge cycles and downtime periods, are highly dependent on on the PV and BESS size, highlighting therefore the need for a detailed analysis of their impact during the sizing optimization process.

Finally, the bottom frame in Figure 7 shows the power exchanged with the grid. According to Equation (1), positive values indicate power consumption (e.g., last 3 days in Figure 7), while negative values indicate power injected into the grid, i.e., when the battery cannot store the surplus of generation (e.g., first 4 days in the figure). As evident from these patterns, the sizing of the PV-BESS system has a significant impact on the exchange of power with the grid and thus on the economic performance of the system.

Based on the system model described in Section 2, it is essential to define quantitative performance parameters that not only take into account both energy and economic aspects, but also allow a direct evaluation of the system performance.

3.1. System Performance Parameters

System energy performance evaluation is based on two parameters: self-consumption (λ_{SC}) and self-sufficiency (λ_{SS}). Self-consumption is the share of the total PV-generated energy that is directly consumed locally. In other words, λ_{SC} quantifies the amount of PV energy utilized on-site rather than exported to the grid on annual basis. Self-sufficiency, on the other hand, refers to the degree to which the on-site PV generation satisfies the load energy demand. λ_{SS} indicates how much of the total energy demand is covered by the PV system. The related formulas are reported in Equations (14) and (15):

$$\lambda_{SC} = 1 - \frac{E_G^-}{E_{PV}} \tag{14}$$

$$\lambda_{SS} = 1 - \frac{E_G^+}{E_{EV}} \tag{15}$$

where E_G^+ and E_G^- are the annual energy purchased from and supplied to the grid, respectively. E_{PV} is the energy produced by the PV system and E_{EV} is the energy absorbed by the charging station on annual basis.

Self-consumption and self-sufficiency vary in the range [0, 1] and exhibit complementary behavior: $\lambda_{SC} = 1$ only if the system does not export energy to the grid, while $\lambda_{SS} = 1$ if the system does not import energy from the grid (totally grid-independent). The value of these parameters is influenced by the sizing of the system. For example, increasing PV size has a positive impact on self-sufficiency by reducing the amount of energy absorbed from the grid. However, PV-oversizing results in a higher amount of energy being injected into the grid, which ultimately reduces self-consumption. On the other hand, since BESS operations reduce grid power exchanges (both E_G^+ and E_G^-), increasing battery size results in higher values of both λ_{SC} and λ_{SS}.

The economic performance of the system is assessed through the levelized cost of energy. The LCOE (θ_{LCOE}) represents the average cost of energy incurred by the charging infrastructure operator delivering energy to EV users, over the lifetime of the system. The greater the reduction in LCOE due to the introduction of the PV-BESS system, the greater the economic benefit of the system. As defined in ref. [39], the LCOE is calculated as follows:

$$\theta_{LCOE} = \frac{\theta_{NPC}}{E_{EV}} \theta_{CRF} \tag{16}$$

The parameter θ_{CRF} in Equation (16) represent the Capital Recovery Factor—CRF that is a financial parameter used to determine the annualized cost of an investment over its lifetime. It converts the total cost of a system (EUR) into an equivalent annual payment (EUR/year) and is obtained by Equation (17):

$$\theta_{CRF} = \frac{r(1+r)^{y_{sys}}}{(1+r)^{y_{sys}} - 1} \tag{17}$$

where r is the discount rate, representing the rate used to discount future cost to their present value, and y_{sys} is the system lifetime, which is chosen equivalent to the PV system lifetime because, after a certain period, the photovoltaic components reach the end of their functional life, making it economically unfeasible to maintain the system [40].

In Equation (16), θ_{NPC} is the Net Present Cost—NPC and represents the total present value of all costs associated with the system over its lifetime, including capital and operative costs. The NPC is given by:

$$\theta_{NPC} = C_{PV} + C_B + \frac{C_G^+ - C_G^-}{\theta_{CRF}} \tag{18}$$

where C_{PV} and C_B are the PV and the BESS cost, respectively:

$$C_{PV} = C_{PV}^{CAP} + C_{PV}^{OM} \tag{19}$$

$$C_B = C_B^{CAP} + C_B^{OM} + C_B^R \tag{20}$$

The capital cost and operation & maintenance (O&M) costs are included in the PV and BESS cost. The BESS cost also takes into account the replacement cost, as BESS typically have shorter lifetimes than PV. Therefore, to accurately account for all costs incurred over the entire system lifetime, the additional costs associated with BESS replacements are included. The therm $C_G^+ - C_G^-$ represents the balance between the cost of energy purchased from the grid and the revenue from energy sold back to the grid, as calculated in Section 2.4. The θ_{NPC} of the system is thus the sum of the PV and BESS costs, plus the difference between the cost of energy purchased and the revenue from energy sold. Revenues from EV charging were not included in the optimization, as the user charging price is assumed to be constant and independent of the PV–BESS configuration.

The capital costs C_{PV}^{CAP} and C_B^{CAP} are calculated in Equations (21) and (22) considering the PV-BESS size, and their specific cost, i.e., c_{PV} in EUR/kWp and c_B in EUR/kWh, respectively, for PV and BESS:

$$C_{PV}^{CAP} = c_{PV} \cdot S_{PV} \tag{21}$$

$$C_B^{CAP} = c_B \cdot S_B \tag{22}$$

The operation and maintenance costs for both the PV and BESS systems are calculated by considering the discount rate and the system lifetime. The C_{PV}^{OM} is given by:

$$C_{PV}^{OM} = c_{PV}^{OM} S_{PV} \cdot \sum_{n=1}^{y_{sys}} \left(\frac{1}{1+r}\right)^n \tag{23}$$

where c_{PV}^{OM} is the annual O&M cost (EUR/kWp/year) of the PV plant. Similarly, the O&M cost for the BESS is calculated as:

$$C_B^{OM} = c_B^{OM} \cdot \sum_{n=1}^{y_{sys}} \left(\frac{1}{1+r}\right)^n \tag{24}$$

where c_B^{OM} is the annual O&M cost of the battery system (EUR/year).

The replacement cost of the BESS is obtained by determining how many replacements are required during the system's lifetime, which is obtained by dividing the total system lifetime by the battery's lifetime y_B, obtained as described in the BESS Degradation Model Section, and calculating the cost of each replacement. Since the resulting number of replacements is typically not an integer, it includes both complete replacements and a fractional replacement at the end of the system's lifetime. The formula for the replacements cost is:

$$C_B^R = C_B^{CAP} \cdot \sum_{i=1}^{m-1} \frac{1}{(1+r)^{i \cdot y_B}} \tag{25}$$

where m is the number of battery replacements during the system's lifetime.

The parameters relevant to the PV-BESS system's economic analysis are summarized in Table 3.

Table 3. System economic parameters and lifetime.

Parameter	Value	Reference
c_{PV}^{OM}	7.7 EUR/kWp/year	[41]
c_B^{OM}	60 EUR/year	[42]
c_{PV}	1100 EUR/kWp	[43]
c_B	350 EUR/kWh	[44]
r	3.4%	[45]
y	25 years	[40]

Economic performance is strongly influenced by the PV-BESS system size. Larger PV systems increase the overall system cost but help lower the expenses associated with purchasing energy from the grid. Similarly, larger BESS size raise the system's cost but increases economic independence from network, reducing system operating costs. The challenge of this work is to provide a method to optimize the performance of the system from both an energy and economic point of view.

3.2. Multi-Objective Optimization

The goal of the sizing optimization process is to determine the pair (S_{PV}, S_{BESS}) that maximizes the system performances. It is possible to consider the previous performance parameters and define two different objective functions. From the energy point of view, the information provided by the parameters λ_{SC} and λ_{SS} are included within the energy objective function, defined as follows:

$$\Lambda = \lambda_{SC} \cdot \lambda_{SS} \tag{26}$$

As described in Section 3.1, λ_{SC} and λ_{SS} are two parameters that range from 0 to 1 and exhibit complementary behavior with respect to system size. When analyzed individually, λ_{SC} is only indicative of system over-sizing, while λ_{SS} is only indicative of under-sizing. The objective Λ in Equation (26) also varies between 0 and 1, but only reaches high values when both λ_{SC} and λ_{SS} are high. This property allows Λ to encapsulate the performance aspects of both λ_{SC} and λ_{SS}, providing a unified measure of both over-sizing and under-sizing of the system. In other words, $\Lambda = 1$ is only achieved when the system does not export or import power to/from the grid.

On the other side, the LCOE is employed to assess the economic performance of the system. This parameter is expressed in relative terms by normalizing it with respect to

the average annual energy purchase price, $c_{\text{buy}}^{\text{av}}$. The corresponding economic objective function is defined in Equation (27):

$$\Theta = \frac{\theta_{\text{LCOE}}}{c_{\text{buy}}^{\text{av}}} \tag{27}$$

If $\Theta < 1$, it indicates that the PV-BESS system is economically advantageous, as the cost of energy is lower than the standard case, i.e., without PV-BESS, where the energy cost is equal to $c_{\text{buy}}^{\text{av}}$.

To prevent negative values of Θ, which would correspond to a gain rather than an energy cost, the selling price is set $c_{\text{sell}} = 0$. This approach avoid that the objective function may favor over-sizing the PV system to maximize revenue from energy sales, thereby deviating from the study's primary goal.

The target of the PV-BESS sizing optimization is to find the solutions (S_{PV}, S_{BESS}) that maximize Λ and minimize Θ. The multi-objective optimization (MOO) problem is described in Equation (28):

$$\begin{cases} \min\limits_{S_{\text{PV}}, S_{\text{B}}} F(S_{\text{PV}}, S_{\text{B}}) = [-\Lambda, \Theta] \\ S_{\text{PV}} \in \Omega_{\text{PV}} \\ S_{\text{B}} \in \Omega_{\text{B}} \end{cases} \tag{28}$$

In order to explore PV-BESS combination compatible with the usual car park size, the range of feasible solutions are $\Omega_{\text{PV}} \in [0, 500]$ kWp for PV and $\Omega_{\text{B}} \in [0, 500]$ kWh for BESS size.

MOO is a branch of optimization focused on solving problems that require the simultaneous optimization of multiple objectives. The two objective functions are often in conflict with each other. For example, higher values of S_{PV} and S_{B} improve Λ but increase capital costs, thereby negatively impacting Θ. As a result, there is typically no single optimal solution, but rather a set of optimal solutions. This set is known as "Pareto front" and consists of all the $[S_{PV}, S_B]$ pairs for which Θ cannot be decreased without reducing Λ, and vice versa.

MOO problems can be addressed using various algorithms to find solutions belonging to the Pareto front, identified with ε. In this work, three of the most widely adopted metaheuristic methods for MOO were considered and compared: NSGA-II, MOEA/D, and MOPSO. These algorithms were selected as they represent three distinct paradigms of multi-objective search: evolutionary selection (NSGA-II), decomposition-based optimization (MOEA/D), and swarm intelligence (MOPSO).

To perform the comparison, each algorithm underwent a preliminary parameter tuning phase to identify algorithm-specific optimal configurations. The optimization problem was then solved using each algorithm implemented in the pymoo Python library (version 0.6.1.5), with all algorithms executed under identical structural conditions (population size, number of generations, random seed management) to ensure reproducibility and fair comparison. The resulting main parameter configurations are summarized in Table 4.

A population size of 100 and 20 generations was selected as a trade-off between exploration capability and computational cost. Preliminary convergence tests confirmed that fitness stabilization was achieved after approximately 10–15 generations, with 20 generations providing a safety margin for robust convergence. Each algorithm was executed for ten independent runs using different random seeds to account for stochastic variability. The performance of each algorithm was evaluated by computing the Hypervolume (HV) indicator, which quantifies both convergence and diversity of the Pareto front. Since the problem is formulated in minimization mode as $[-\Lambda, \Theta]$, the nadir point (worst-case scenario) is

(0, 1). The reference point was set to (0, 1.1), scaling the nadir by a factor of 1.1 to ensure numerical robustness and prevent boundary effects [46]. For each algorithm, the mean and standard deviation of the HV across the ten runs were calculated, together with the average execution time.

Table 4. Parameters adopted for the three multi-objective algorithms.

Parameter	NSGA-II	MOEA/D	MOPSO
Population Size [1]	100	100	100
Number of Generations	20	20	20
Crossover Probability	0.98	0.92	-
Crossover Distribution Index	15	15	-
Mutation Probability	0.2	0.2	-
Mutation Distribution Index	20	20	-
Inertia Weight (w)	-	-	0.7
Acceleration Coefficients (c_1, c_2)	-	-	1.5, 1.5

[1] For MOEA/D, the population size corresponds to the number of reference directions.

A Kruskal–Wallis H-test was performed on the HV distributions across the three algorithms ($n = 10$ runs each, $\alpha = 0.05$). The test yielded $H = 19.42$, $p < 0.001$, indicating statistically significant differences. Pairwise Mann–Whitney U tests with Bonferroni correction ($\alpha_{\text{corrected}} = 0.0167$) revealed that NSGA-II and MOPSO achieve statistically equivalent HV values ($p = 0.734$), with mean values of 0.3552 ± 0.0002 and 0.3556 ± 0.0007, respectively. Conversely, MOEA/D exhibited significantly lower performance ($p < 0.001$ against both NSGA-II and MOPSO), with mean HV of 0.3533 ± 0.0012. Despite comparable Pareto front quality between NSGA-II and MOPSO, NSGA-II demonstrated superior stability across runs (lower standard deviation) and required 5.6% less computation time. Therefore, NSGA-II was selected as the reference algorithm for all subsequent analyses.

Having established NSGA-II as the optimal algorithm, the analysis now focuses on identifying the best design solution from the resulting Pareto front. By means of the Pareto front, it is possible to identify three significant points: $\varepsilon_\Lambda = [\Lambda^*, \Theta]$, which represents the Pareto solution with the highest energy performance Λ; $\varepsilon_\Theta = [\Lambda, \Theta^*]$, which is the Pareto solution with the best economic performance Θ. The third is the ideal point $\varepsilon^*_{\Lambda\Theta} = [\Lambda^*, \Theta^*]$, which can be obtained by the intersection of ε_Λ and ε_Θ. The ideal point is, therefore, a non-feasible solution that represents the best possible values for each objective, meaning that it achieves the highest performance for both energy and economic objective functions. However, this point cannot be realized in practice because it lies outside the feasible solution space.

Since the goal of this study is to determine the optimal size of the PV+BESS system that simultaneously maximizes energy performance and economic profitability, the optimal point between the Pareto front was chosen by finding the Pareto point that minimizes the Euclidean distances from the ideal point [47]. Euclidean distance is a geometric distance measure that quantifies the distance between two points in a multidimensional space. In the context of this study, the Euclidean distance d^* between the $\varepsilon^*_{\Lambda\Theta}$ and the closest point on the Pareto front $\varepsilon_{\Lambda\Theta}$ is calculated in Equation (29):

$$d^* = \min \sqrt{(\Lambda_j - \Lambda^*)^2 + (\Theta_j - \Theta^*)^2}, \quad j = 1, 2, \ldots, m \tag{29}$$

where Λ_j and Θ_j are the values of the objective functions for the j-th point on the Pareto front and m is the number of solution composing the Pareto front.

4. Result and Discussion

This section outlines the economic and energy benefits of integrating the PV-BESS system with EV charging infrastructure, highlighting the difference across the various locations and park sizes. Figure 8 presents the Pareto fronts for the four different parking locations under the three sizes, small, medium, and large, arranged from left to right. The points of interest on the Pareto front, such as ε_{Λ}, ε_{Θ}, $\varepsilon^{*}_{\Lambda\Theta}$, and $\varepsilon_{\Lambda\Theta}$, are highlighted in each graph. The PV-BESS sizing results and the economic and energy performances of each point of interest are also summarized in Table 5.

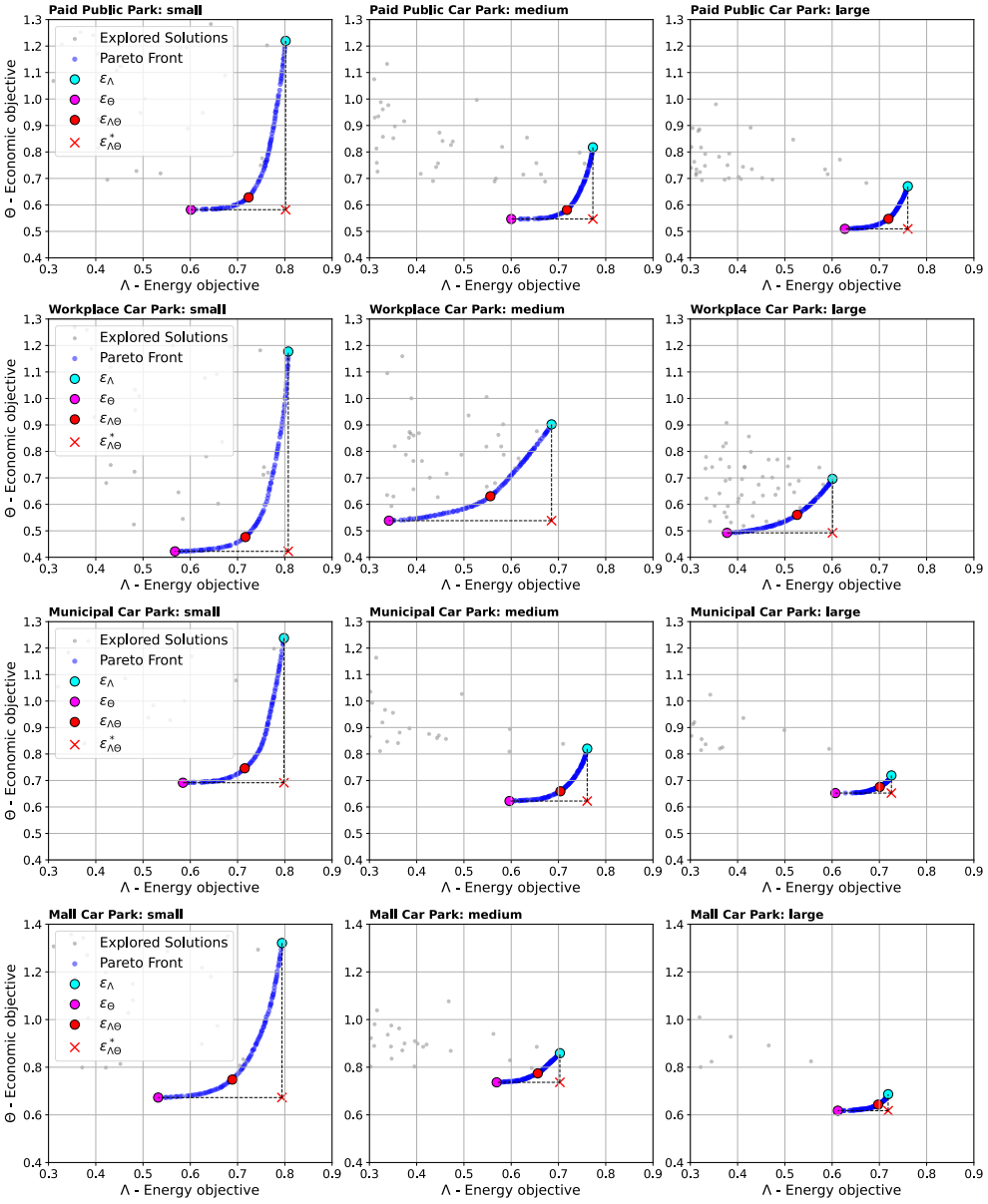

Figure 8. Pareto fronts for different car park locations and footfall scenarios: paid public car park, workplace car park, municipal car park, and mall car park.

As can be seen, the charging location, and therefore the charging power profile, have a significant impact on the energy independency and the economic effectiveness of the PV system with storage. Furthermore, the car park size also impacts the system's performance. For each scenarios, as the size of the car park increase, the spread of the Pareto front decrease. Since the same domain is considered across all scenarios, oversized PV-BESS systems in smaller car parks are economically less attractive. This is because the additional

costs associated with larger systems outweigh the benefits of reducing the share of energy absorbed from the grid. As a result, the front is vertically extended. Furthermore, since larger PV-BESS systems enhance the energy efficiency of the system, the front also extends horizontally. Conversely, larger loads within the same domain lead to a tighter Pareto front.

Table 5. Sizing and performance results for the best solution point, best economic performance point, and best energy performance point, for each location and size.

Location	Scenario	$\varepsilon_{\Lambda\Theta}$		S_{PV} (kWp)	S_B (kWh)	ε_{Θ}		S_{PV} (kWp)	S_B (kWh)	ε_{Λ}		S_{PV} (kWp)	S_B (kWh)
		Λ	Θ			Λ	Θ^*			Λ^*	Θ		
Public car park	small	0.72	0.63	49	127	0.60	0.58	59	86	0.80	1.21	49	500
	medium	0.72	0.58	95	202	0.60	0.55	115	139	0.77	0.82	93	500
	large	0.72	0.54	144	268	0.63	0.51	172	186	0.76	0.67	140	500
Workplace car park	small	0.72	0.48	45	54	0.57	0.42	60	17	0.80	1.18	46	500
	medium	0.56	0.63	110	176	0.34	0.54	164	18	0.69	0.9	93	500
	large	0.53	0.56	211	212	0.38	0.49	268	8	0.60	0.70	188	500
Municipal car park	small	0.72	0.75	52	180	0.58	0.69	62	128	0.80	1.24	51	500
	medium	0.70	0.66	100	279	0.60	0.62	123	214	0.76	0.82	100	500
	large	0.70	0.68	151	427	0.61	0.65	175	346	0.73	0.72	143	500
Mall car park	small	0.69	0.75	47	163	0.53	0.67	51	91	0.79	1.32	46	500
	medium	0.66	0.77	114	388	0.57	0.74	133	301	0.70	0.86	107	500
	large	0.70	0.64	164	423	0.61	0.62	196	356	0.72	0.69	156	500

As reported in Table 5, among the considered locations, the best energy performance result is obtained for the paid public car park. This result can be explained as, in this location, the load distribution is more concentrated during daytime hours and well-balanced throughout the day. This allows for good self-sufficiency of the system, with no excessive peak demands that would require additional energy from the grid. Furthermore, the unchanged load between weekdays and weekends, allows for a well-sized system that performs efficiently throughout the entire week, avoiding over- or under-sizing due to fluctuations in demand between weekdays and weekends. With regard to economic effectiveness, for all the considered sizes of the public car park, the chosen solution on the Pareto front $\varepsilon_{\Lambda\Theta}$ results to present an high energy cost saving, 37%, 42%, and 46% for small, medium, and large park sizes, respectively. Despite the peak load occurring in the evening, when PV power is no longer available and a larger BESS is required, there remains a substantial energy cost saving, as most of the load is concentrated during daylight hours.

The workplace car park scenario, at the $\varepsilon_{\Lambda\Theta}$ point, achieves similar economic performance, with energy cost savings of 52%, 37%, and 44% for the low, medium, and high scenarios, respectively. This is due to the alignment of the charging time slot with working hours, featuring a peak demand in the morning when PV production is available and no load during the evening. As a result, a large PV size and a very small BESS capacity are sufficient, leading to a more cost-effective system. With regard to system energy independency, the medium and large scenarios exhibit the worst results among all the considered cases. These low performances can be attributed to two factors: the sharp and sustained morning peak load and the absence of load during weekend. The morning peak, which PV generation and the small BESS capacity cannot fully cover, leading to a higher reliance on grid energy. The second factor is that during the weekend, since the load is absent, once the battery storage is full, all the energy produced by the PV system is fed into the grid, reducing the system self-consumption. However, the small car park scenario achieves good energy performance. In fact, as shown in Figure 3, the peak load in this scenario is modest, since the number of vehicles daily charged is small. In this case, the PV and BESS systems are more effective in meeting the demand, as the smaller battery is better suited to support the load, compensating for the reduced self-consumption during the weekends.

Lower economic performance is observed in the last two parking scenarios: the municipal car park and the mall car park. Regarding the municipal parking, at the $\varepsilon_{\Lambda\Theta}$ point, under the three size scenarios, the economic performance never exceeds a cost saving of 34%, while the energy performance is similar to that of the public car park. The charging hub load profile in this scenario is characterized by a high variance in parking times, including late evenings and peaks during peak traffic hours. The evening load, due to the lack of PV production, negatively impacts economic performance as it must be covered by the BESS energy supply. This requires a larger storage capacity, which increases the overall system cost, while since the BESS size required to meet the load is high, this helps to have high energy performance. Moreover, the reduction in load during the weekend, amounting to −33% compared to weekdays, slightly contributes to the reduction in energy performance. In fact, during weekdays, the higher load decreases self-sufficiency, as grid energy is required to meet demand. Conversely, during the weekend, the lower load reduces self-consumption, as the surplus energy must be injected into the grid.

Finally, in the mall car park scenario, the poorest overall performance was observed. Economic performance was the weakest among all scenarios, and energy performance was also suboptimal, surpassed only by the lower results observed in the workplace scenario. This scenario is characterized by a high flow of users during the daytime, with a moderate increase in the evening hours. In particular, the evening load increase, as observed in the municipal scenario, necessitates a larger battery capacity to supply the load required by the CH, resulting in higher system costs. Evidence of this is the fact that, for both the municipal and mall scenarios, the selected best solution on the Pareto front, $\varepsilon_{\Lambda\Theta}$, results in BESS capacities of 279 kWh and 388 kWh, respectively, which are significantly larger than those required for the first two locations. As far as energy performance is concerned, as shown in the load profile in Figure 3, there are no significant load peaks during the day. However, the reduction in energy efficiency across all scenarios can be attributed to the substantial increase in load during the weekends, i.e., 51% compared to weekdays. This increase impacts not only energy performance but also economic performance, as the higher weekend load necessitates a larger PV-BESS system to accommodate the demand, leading to increased system costs. Furthermore, during the weekdays, when the load is smaller, there is a reduction in the system's self-consumption, while at weekends, when the load is greater, self-sufficiency decreases.

The results discussed above are corroborated by the heat maps in Figure 9. The figure presents energy performance on the left and economic performance on the right, illustrating the outcomes across the optimization domain for the medium car park size scenario at the considered locations.

The energy performance heat maps clearly show that system energy independency improves as the BESS size increases, as larger systems can store and supply greater amounts of energy during operation. On the other hand, regarding the optimal PV size, similar PV sizes were obtained for all scenarios. This is because the PV size primarily depends on the energy required to meet the load, and the energy differences between the scenarios are minimal, as the same number of vehicles is considered. Consequently, the PV sizes remain comparable across scenarios, with the load profile having no significant impact in this regard. This means that, in accordance with Figure 9, the PV system with a capacity of approximately 100 kWp supply an amount of energy equivalent to that required by the charging station in the medium scenario.

As for the economic performance heat maps, the optimal PV size is consistent with that seen in the energy performance heat maps, as oversizing the PV leads to higher costs without any corresponding benefit, since the sale of surplus energy to the grid is not considered. Notably, only in the workplace scenario is the optimal PV size slightly larger

than in the others, as the peak load aligns with the peak PV production, as previously mentioned. The BESS size, however, depends on the specific load profile. The greater the deviation between the load profile and the PV production profile, the larger the battery capacity required, as observed in the municipal and mall car park scenarios.

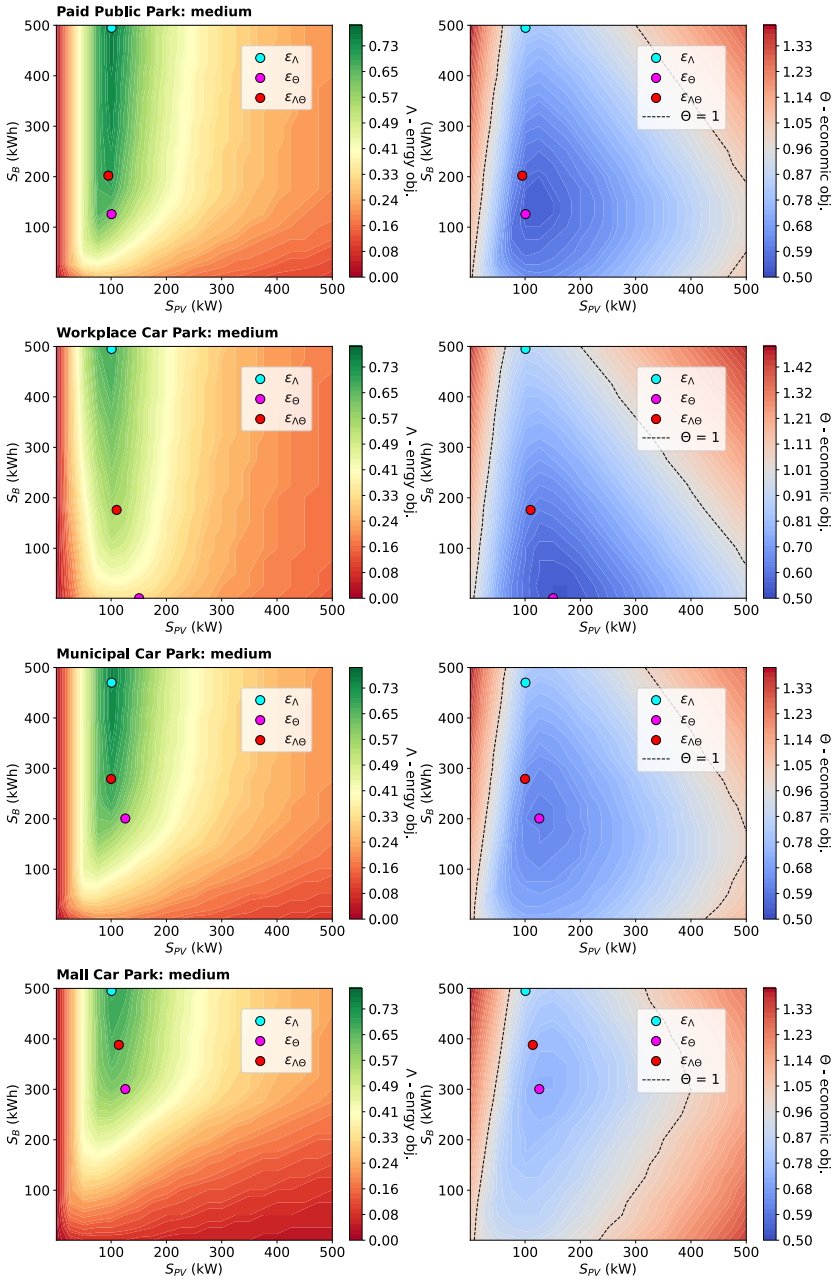

Figure 9. Heat maps showing the energy and economic performance results within the domain of the considered location for the large car park scenario.

Heat maps in Figure 9 confirm that, the overall best performance are achieved by the paid public car park. High energy performance are achieved for a wider range of BESS sizes, as indicated by the broad green area. In the economic heat map, low energy costs are achieved, while overall economic efficiency is maintained across almost the entire domain, as Θ stays below 1 in nearly all areas, indicated by the region within the dashed line. It may also be noted that, even without an energy storage, the economic effectiveness is achieved in almost the entire PV size domain.

With regard to the workplace car park, energy performance turn out to be not high as the previous location but still quite spread for greater values of BESS size. The economic performance clearly shows that, since the load profile match the PV production profile, the minimum value of the cost of energy is achieved with almost no battery storage. Moreover, Θ is below 1 for all the domain of PV when S_B is equal to 0.

In the considered domain, municipal car park location, achieved similar energy performance with respect to public car park but has lower energy performance since the BESS required is higher, as evidenced by the economic performance heat map.

Finally, the mall car park scenario demonstrates a relatively high maximum energy performance within the domain, outperforming the workplace scenario, but with a narrower range of good energy performance values, confined mainly to larger BESS sizes. This results in poor energy performance for the PV system without battery storage, highlighting once again the poor match between the PV profile and the load profile in this scenario. As a consequence, a significantly large BESS storage capacity is required, leading to higher Θ, as shown by the economic performance heat map.

The results obtained can be summarized as follows. The paid public par park achieves the best overall performance, with economic savings of up to 46%. The system is highly self-sufficient, minimizing grid reliance, and its consistent load profile throughout the week leads to efficient system sizing. The workplace car park also demonstrates excellent economic savings, up to 52%, but low energy performance, especially in medium and large scenarios due to the high peak load in the morning and the lack of load at weekends. The municipal car park has lower economic savings, never exceeding 34%, despite having similar energy performance to the public car park. This is because more battery storage is required to meet evening load demands, increasing costs and reducing performance. Finally, the mall par park shows the weakest overall performance, while it achieves good energy performance, it requires a significantly larger battery to cover evening peak loads, leading to higher costs.

5. Conclusions

This study proposed a multi-objective optimization method for the optimal sizing of PV-BESS systems to support EV charging hubs. The framework aimed to maximize both energy and economic system performance. The energy objective function, defined as the product of system self-consumption and self-sufficiency, represent the energy independency of the CH from the grid. Economic objective function, on the other hand, was defined as the LCOE, relativized to the average energy purchase price. Four distinct charging station locations, representing different urban and functional contexts, specifically, public car park, workplace car park, municipal car park, and mall car park, were analyzed to evaluate the impact of location and CH size (small, medium, and large) on system performance. A battery degradation model was implemented for realistic lifetime estimations. The resulting multi-objective problem was solved using the NSGA-II algorithm, selected after comparative testing with MOEA/D and MOPSO demonstrated its superior stability and computational efficiency while maintaining equivalent Pareto front quality.

The achieved results revealed that locations with well-aligned load distributions, such as the paid public car park, demonstrate superior overall performance due to efficient utilization of PV energy and reduced storage requirements. Specifically, for the paid public car park scenario, an average energy cost saving of 42% was obtained, while the energy independency ($\varepsilon_{\Lambda\Theta}$) was 0.72 for each CH size. Conversely, scenarios with mismatched load and generation profiles, like the mall car park, require larger battery systems to achieve comparable energy performance, with an average $\varepsilon_{\Lambda\Theta}$ of 0.68, leading to higher costs. For the mall car park scenario, in fact, the average energy cost saving obtained was 28%,

which is 33% lower compared to the paid public car park. Finally, pronounced load peaks were identified as the primary cause of the poor energy performance in the analyzed scenarios. Specifically, the workplace scenario, characterized by a significant morning load peak, achieved the lowest performance, with an average $\varepsilon_{\Lambda\Theta}$ of 0.6 across the three considered sizes. With regard to the PV-BESS system sizes among the considered scenarios, while the PV size depends more on the energy required by the specific load than on the daily load profile, the BESS size is strongly correlated with the load profile. The smallest BESS sizes were found for the paid public and workplace parking lot scenarios, with PV-BESS system sizes of 144 kWp–268 kWh and 211 kWp–212 kWh, respectively, for the large parking lot. In contrast, for the municipal and mall parking scenarios, the optimal system sizes for the large car park are 151 kWp–427 kWh and 164 kWp–423 kWh, with BESS capacities approximately double those of the previous scenarios.

These findings underscore the importance of tailored system sizing to maximize efficiency, sustainability and cost-effectiveness in EV charging infrastructures. Future developments of this work could include the implementation of Vehicle-to-Grid functionality. In such a scenario, EVs would operate as distributed energy storage units, providing bidirectional power exchange with the grid and enhancing system flexibility. This capability could reduce the required size of the stationary BESS or alter its optimal operation strategy. In addition, future work will include the modeling of the battery internal resistance growth, represented as a progressive reduction of the battery maximum deliverable power $P_B^{\max}$, to capture the effects of power fade associated with battery aging.

Author Contributions: F.M.T. contributed to conceptualization, methodology, software, validation, formal analysis, investigation, data curation, and writing—original draft. F.L.F. contributed to conceptualization, methodology, software, validation, formal analysis, investigation, data curation, writing—review and editing, and supervision. M.R. contributed to methodology, data curation, writing—review and editing, visualization, and supervision. All authors have read and agreed to the published version of the manuscript.

Funding: This work was funded by European Union under the National Recovery and Resilience Plan PNRR-Missione 4-Componente 2, Investimento 1.5 "Creazione e rafforzamento di Ecosistemi dell'innovazione, costruzione di leader territoriali di R&S" D.D. 3277 del 30 December 2021, research project "ECOSISTER-Ecosystem for Sustainable Transition in Emilia-Romagna", Code ECS00000033, CUP J33C22001240001.

Data Availability Statement: The original contributions presented in this study are included in the article material. Further inquiries can be directed to the corresponding author.

Conflicts of Interest: Author Francesco Lo Franco was employed by the company Syniergy S.r.l. The remaining authors declare that the research was conducted in the absence of any commercial or financial relationships that could be construed as a potential conflict of interest.

References

1. International Energy Agency (IEA). Global EV Data Explorer. 2024. Available online: https://www.iea.org/data-and-statistics/data-tools/global-ev-data-explorer (accessed on 30 October 2024).
2. International Energy Agency (IEA). Europe—Data and Analysis. 2024. Available online: https://www.iea.org/regions/europe (accessed on 14 January 2025).
3. Ricerca sul Sistema Energetico (RSE). Impatto Delle Infrastrutture di Ricarica Sulla Rete Elettrica di Distribuzione. 2022. Available online: https://www.rse-web.it/ (accessed on 12 December 2024).
4. The Guardian. France to Require All Large Car Parks to be Covered by Solar Panels. 2022. Available online: https://www.theguardian.com/world/2022/nov/09/france-to-require-all-large-car-parks-to-be-covered-by-solar-panels (accessed on 12 December 2024).
5. Wang, H.; Wang, J.; Piao, Z.; Meng, X.; Sun, C.; Yuan, G.; Zhu, S. The Optimal Allocation and Operation of an Energy Storage System with High Penetration Grid-Connected Photovoltaic Systems. *Sustainability* **2020**, *12*, 6154. [CrossRef]

6. Khawaja, Y.; Giaouris, D.; Patsios, H.; Dahidah, M. Optimal cost-based model for sizing grid-connected PV and battery energy system. In Proceedings of the 2017 IEEE Jordan Conference on Applied Electrical Engineering and Computing Technologies (AEECT), Aqaba, Jordan, 11–13 October 2017; pp. 1–6. [CrossRef]
7. Dai, Q.; Liu, J.; Wei, Q. Optimal Photovoltaic/Battery Energy Storage/Electric Vehicle Charging Station Design Based on Multi-Agent Particle Swarm Optimization Algorithm. *Sustainability* **2019**, *11*, 1973. [CrossRef]
8. Liu, G.; Xue, Y.; Chinthavali, M.S.; Tomsovic, K. Optimal Sizing of PV and Energy Storage in an Electric Vehicle Extreme Fast Charging Station. In Proceedings of the 2020 IEEE Power & Energy Society Innovative Smart Grid Technologies Conference (ISGT), Washington, DC, USA, 17–20 February 2020; pp. 1–5. [CrossRef]
9. Zhou, L.; Zhang, Y.; Lin, X.; Li, C.; Cai, Z.; Yang, P. Optimal Sizing of PV and BESS for a Smart Household Considering Different Price Mechanisms. *IEEE Access* **2018**, *6*, 41050–41059. [CrossRef]
10. Yan, D.; Ma, C. Optimal Sizing of A PV Based Electric Vehicle Charging Station Under Uncertainties. In Proceedings of the IECON 2019—45th Annual Conference of the IEEE Industrial Electronics Society, Lisbon, Portugal, 14–17 October 2019; Volume 1, pp. 4310–4315. [CrossRef]
11. Nafeh, A.E.S.A.; Omran, A.E.F.A.; Elkholy, A.; Yousef, H. Optimal economical sizing of a PV-battery grid-connected system for fast charging station of electric vehicles using modified snake optimization algorithm. *Results Eng.* **2024**, *21*, 101965. [CrossRef]
12. Korjani, S.; Serpi, A.; Damiano, A. A Genetic Algorithm Approach for Sizing Integrated PV-BESS Systems for Prosumers. In Proceedings of the 2020 2nd IEEE International Conference on Industrial Electronics for Sustainable Energy Systems (IESES), Cagliari, Italy, 1–3 September 2020; Volume 1, pp. 151–156. [CrossRef]
13. Kelepouris, N.S.; Nousdilis, A.I.; Bouhouras, A.S.; Christoforidis, G.C. Enhancing Self-Sufficiency in Buildings with Hybrid PV-Battery Systems and Demand Side Management: A Sizing Tool. In Proceedings of the 2021 IEEE International Conference on Environment and Electrical Engineering and 2021 IEEE Industrial and Commercial Power Systems Europe, Bari, Italy, 7–10 September 2021; pp. 1–6. [CrossRef]
14. Fang, C.; Zhao, X.; Xu, Q.; Li, Y.; Wang, H.; Feng, D.; Zhang, K.; Zhou, Y. Optimal Battery and PV Sizing of Charging Stations Considering Battery Dynamic Characteristics. In Proceedings of the 2021 Power System and Green Energy Conference (PSGEC), Shanghai, China, 20–22 August 2021; pp. 453–459. [CrossRef]
15. Lo Franco, F.; Ricco, M.; Cirimele, V.; Apicella, V.; Carambia, B.; Grandi, G. Electric Vehicle Charging Hub Power Forecasting: A Statistical and Machine Learning Based Approach. *Energies* **2023**, *16*, 2076. [CrossRef]
16. Leone, C.; Longo, M.; Fernández-Ramírez, L.M.; García-Triviño, P. Multi-Objective Optimization of PV and Energy Storage Systems for Ultra-Fast Charging Stations. *IEEE Access* **2022**, *10*, 14208–14224. [CrossRef]
17. Vermeer, W.; Mouli, G.R.C.; Bauer, P. Optimal Sizing and Control of a PV-EV-BES Charging System Including Primary Frequency Control and Component Degradation. *IEEE Open J. Ind. Electron. Soc.* **2022**, *3*, 236–251. [CrossRef]
18. Islam, M.S.; Mithulananthan, N.; Bhumkittipich, K. Feasibility of PV and battery energy storage based EV charging in different charging stations. In Proceedings of the 2016 13th International Conference on Electrical Engineering/Electronics, Computer, Telecommunications and Information Technology (ECTI-CON), Chiang Mai, Thailand, 28 June–1 July 2016; pp. 1–6. [CrossRef]
19. Alshammari, N.F.; Samy, M.M.; Barakat, S. Comprehensive Analysis of Multi-Objective Optimization Algorithms for Sustainable Hybrid Electric Vehicle Charging Systems. *Mathematics* **2023**, *11*, 1741. [CrossRef]
20. Leone, C.; Peretti, C.; Paris, A.; Longo, M. Photovoltaic and battery systems sizing optimization for ultra-fast charging station integration. *J. Energy Storage* **2022**, *52*, 104995. [CrossRef]
21. Abe, C.F.; Dias, J.B.; Notton, G.; Poggi, P. Computing Solar Irradiance and Average Temperature of Photovoltaic Modules from the Maximum Power Point Coordinates. *IEEE J. Photovolt.* **2020**, *10*, 655–663. [CrossRef]
22. Huld, T.; Müller, R.; Gambardella, A. A new solar radiation database for estimating PV performance in Europe and Africa. *Sol. Energy* **2012**, *86*, 1803–1815. [CrossRef]
23. Sun, V.; Asanakham, A.; Deethayat, T.; Kiatsiriroat, T. Evaluation of nominal operating cell temperature (NOCT) of glazed photovoltaic thermal module. *Case Stud. Therm. Eng.* **2021**, *28*, 101361. [CrossRef]
24. Bortolini, M.; Gamberi, M.; Graziani, A. Technical and economic design of photovoltaic and battery energy storage system. *Energy Convers. Manag.* **2014**, *86*, 81–92. [CrossRef]
25. Raszmann, E.; Baker, K.; Shi, Y.; Christensen, D. Modeling stationary lithium-ion batteries for optimization and predictive control. In Proceedings of the 2017 IEEE Power and Energy Conference at Illinois (PECI), Champaign, IL, USA, 23–24 February 2017; pp. 1–7. [CrossRef]
26. Akeyo, O.M.; Rallabandi, V.; Jewell, N.; Patrick, A.; Ionel, D.M. Parameter Identification for Cells, Modules, Racks, and Battery for Utility-Scale Energy Storage Systems. *IEEE Access* **2020**, *8*, 215817–215826. [CrossRef]
27. Lo Franco, F.; Morandi, A.; Raboni, P.; Grandi, G. Efficiency comparison of DC and AC coupling solutions for large-scale PV+BESS power plants. *Energies* **2021**, *14*, 4823. [CrossRef]

28. Noyanbayev, N.; Forsyth, A.; Feehally, T. Efficiency analysis for a grid-connected battery energy storage system. *Mater. Today Proc.* **2018**, *5*, 22811–22818. [CrossRef]
29. Stroe, D.I.; Swierczynski, M.; Stroe, A.I.; Teodorescu, R.; Laerke, R.; Kjaer, P.C. Degradation behaviour of Lithium-ion batteries based on field measured frequency regulation mission profile. In Proceedings of the 2015 IEEE Energy Conversion Congress and Exposition (ECCE), Montreal, QC, Canada, 20–24 September 2015; pp. 14–21. [CrossRef]
30. Wang, J.; Liu, P.; Hicks-Garner, J.; Sherman, E.; Soukiazian, S.; Verbrugge, M.; Tataria, H.; Musser, J.; Finamore, P. Cycle-life model for graphite-LiFePO4 cells. *J. Power Sources* **2011**, *196*, 3942–3948. [CrossRef]
31. Stroe, D.I.; Świerczyński, M.; Stan, A.I.; Teodorescu, R.; Andreasen, S.J. Accelerated Lifetime Testing Methodology for Lifetime Estimation of Lithium-Ion Batteries Used in Augmented Wind Power Plants. *IEEE Trans. Ind. Appl.* **2014**, *50*, 4006–4017. [CrossRef]
32. Wu, C.H.; Jhan, J.Z.; Ko, C.H.; Kuo, C.C. Evaluating and Analyzing the Degradation of a Battery Energy Storage System Based on Frequency Regulation Strategies. *Appl. Sci.* **2022**, *12*, 6111. [CrossRef]
33. Akpinar, K.N.; Gundogdu, B.; Ozgonenel, O. A novel cycle counting perspective for energy management of grid integrated battery energy storage systems. *Energy Rep.* **2023**, *9*, 123–131. [CrossRef]
34. Alam, M.J.E.; Saha, T.K. Cycle-life degradation assessment of Battery Energy Storage Systems caused by solar PV variability. In Proceedings of the 2016 IEEE Power and Energy Society General Meeting (PESGM), Boston, MA, USA, 17–21 July 2016; pp. 1–5. [CrossRef]
35. Chen, Y.; Ni, J.; Li, H.; Yang, F.; Yin, G. Enhanced Research on the Determination of Aging Degree in Embedded Energy Storage Configurations Utilizing the Rain Flow Counting Method. In Proceedings of the 2024 43rd Chinese Control Conference (CCC), Kunming, China, 28–31 July 2024; pp. 2160–2164. [CrossRef]
36. Gestore dei Mercati Energetici. GME Profile—Italian Electricity Market Operator. 2024. Available online: https://www.mercatoelettrico.org/en-us/Home/GME/GMEProfile (accessed on 3 December 2024).
37. Eurostat. Electricity Prices for Household Consumers—NRG_PC_204. 2024. Available online: https://ec.europa.eu/eurostat/databrowser/view/nrg_pc_204/default/table?lang=en (accessed on 14 October 2024).
38. ARERA—Autorità di Regolazione per Energia Reti e Ambiente. Relazione Annuale Sullo Stato Dei Servizi e Sull'Attività Svolta. 2024. Available online: https://www.arera.it/fileadmin/allegati/relaz_ann/24/RA24_vol1.pdf (accessed on 16 December 2024).
39. Sun, B. A multi-objective optimization model for fast electric vehicle charging stations with wind, PV power and energy storage. *J. Clean. Prod.* **2021**, *288*, 125564. [CrossRef]
40. Khezri, R.; Mahmoudi, A.; Haque, M.H. A Demand Side Management Approach For Optimal Sizing of Standalone Renewable-Battery Systems. *IEEE Trans. Sustain. Energy* **2021**, *12*, 2184–2194. [CrossRef]
41. NREL. *Best Practices for Operation and Maintenance of Photovoltaic and Energy Storage Systems*, 3rd ed.; U.S. Department of Energy (DOE): Golden, CO, USA, 2019. Available online: https://www.nrel.gov/docs/fy19osti/73822.pdf (accessed on 14 October 2024).
42. Brinsmead, T.; Graham, P.; Hayward, J.; Ratnam, E.; Reedman, L. *Future Energy Storage Trends: An Assessment of the Economic Viability, Potential Uptake, and Impacts of Electrical Energy Storage on the NEM 2015–2035*; Technical Report; CSIRO: Melbourne, Australia, 2015; Report Prepared for the Australian Energy Market Commission (AEMC).
43. Fall, S.; Dreves, H. *U.S. Solar Photovoltaic System and Energy Storage Cost Benchmarks, with Minimum Sustainable Price Analysis: Q1 2023*; Technical Report; National Renewable Energy Laboratory (NREL): Golden, CO, USA, 2023.
44. Bielewski, M.; Pfrang, A.; Bobba, S.; Kronberga, A.; Georgakaki, A.; Letout, S.; Kuokkanen, A.; Mountraki, A.; Ince, E.; Shtjefni, D.; et al. *Clean Energy Technology Observatory: Batteries for Energy Storage in the European Union—2022 Status Report on Technology Development, Trends, Value Chains and Markets*; Publications Office of the European Union: Luxembourg, 2022; JRC130724. [CrossRef]
45. Trading Economics. Euro Area Interest Rate. 2024. Available online: https://tradingeconomics.com/euro-area/interest-rate (accessed on 4 December 2024).
46. Ishibuchi, H.; Imada, R.; Setoguchi, Y.; Nojima, Y. Reference point specification in hypervolume calculation for fair comparison and efficient search. In Proceedings of the 2017 Genetic and Evolutionary Computation Conference (GECCO'17), Berlin, Germany, 15–19 July 2017; pp. 585–592.
47. Chen, W.; Hu, Z.; Gao, X.; Liu, Y. Simulation and Multi-Objective Optimization of Three-Column Double-Effect Methanol Distillation by NSGA-III Algorithm. *Processes* **2023**, *11*, 1515. [CrossRef]